A&A 376, 1064–1072 (2001)
DOI: 10.1051/0004-6361:20011032
© ESO 2001

Astronomy
&
Astrophysics

The physical conditions in the PDR of W49N*

C. Vastel[1], M. Spaans[2], C. Ceccarelli[3,4], A. G. G. M. Tielens[2], and E. Caux[1]

[1] CESR CNRS-UPS, BP 4346, 31028 Toulouse Cedex 04, France
[2] Kapteyn Astronomical Institute, PO Box 800, 9700 AV Groningen, The Netherlands
[3] Observatoire de Bordeaux, 2 rue de l'Observatoire, BP 89, 33270 Floirac, France
[4] Observatoire de Grenoble, BP 53, 38041 Grenoble Cedex 09, France

Received 24 April 2001 / Accepted 12 July 2001

Abstract. We present ISO-LWS and ground-based SEST observations which probe the Photo Dissociation Region (PDR) of W49N. The ISO-LWS observations consist of low resolution (∼200) grating spectra between 43 μm and 197 μm, and high resolution ($\sim 10^4$) Fabry-Pérot spectra of the [CII] 158 μm and [OI] 63 and 145 μm lines. The SEST observations consist of $C^{16}O$ $J = 1 \rightarrow 0$ and $C^{18}O$ $J = 2 \rightarrow 1$ maps of the region. Using all these observations and with the help of a detailed PDR model, we have determined the physical and chemical structure of the PDR of W49N. We find that only a tiny fraction, 2.5%, of the cloud gas is in the atomic form. This gas has an average density $n = 10^4$ cm^{-3} and a temperature $T \sim 130$ K. The PDR is created by a FUV field $G_0 = 3 \times 10^5$ times brighter than the average FUV interstellar field, which is emitted by the stars associated with the several HII regions inside the cloud. The photoelectric heating efficiency is very low, $\sim 10^{-4}$, relative to other known PDRs, probably because of the relatively high G_0/n ratio. Overall, W49N seems to be one of the youngest giant molecular clouds actively forming stars in the Galaxy, since most of the cloud material is still molecular and dense and not yet dispersed by the several embedded newly formed massive protostars.

Key words. ISM: abundances – ISM: molecules – ISM: atoms – HII regions – ISM: individual: W49N

1. Introduction

The W49N region is one of the most luminous regions of active star formation in the Galaxy. At a distance of ∼11.4 kpc (Gwinn et al. 1992), W49N is located at about the same galactocentric radius as the Sun and generates a total bolometric luminosity of 6.8×10^6 $L_\odot$ (Buckley & Ward-Thompson 1996). Because of extremely high extinction at visible wavelength, this region can only by studied at radio and infrared wavelengths. Maps of W49N in the infrared at 53 μm (Harvey et al. 1977) showed a number of separate condensations each of which is coincident with a radio continuum source (Wynn-Williams 1971; Webster et al. 1971).

Several kinematical models have been proposed to explain the origin of the burst of star formation in the W49N complex. Mufson & Liszt (1977) first proposed a "two cloud collision" model, in which star formation has occurred at the interacting region between two massive molecular clouds. Their CO (2.6 mm), H_2CO (2 cm) and hot ionized gas (H76α) observations are consistent with a picture where a large HII region lies between two massive molecular clouds at velocities of ∼4 and 12 km s^{-1}. Welch et al. (1987) proposed an alternative scenario based on 6 cm continuum, H76α and HCO$^+$ (1–0) observations, in which a single collapsing molecular cloud leads to a rotating ring of at least ten ultracompact HII regions. However, de Pree et al. (1997) complemented these studies with observations of H92α, H66α and H52α and found no evidence of any ordered motions indicating rotation. In addition, Serabyn et al. (1993) detected three dense molecular clumps (two at 12 km s^{-1} and one at 4 km s^{-1}) in the W49N core with their CS and C^{34}S observations, and re-proposed that star formation has been triggered by a cloud-cloud collision, and not by a free-fall collapse.

In this paper, we report observations of several far-infrared and millimeter emission lines in W49N and use the fluxes from these lines to examine the physical properties of the emitting region. The FIR lines of [OI] (63 and 145 μm), [CII] (158 μm), and the rotational lines of CO provide important diagnostic tools for investigation of the physical conditions in Photo-Dissociation Regions

---

Send offprint requests to: C. Vastel,
e-mail: `vastel@cesr.fr`

* Based on observations with ISO, an ESA project with instruments funded by ESA Member States (especially the PI countries: France, Germany, The Netherlands and the UK) with the participation of ISAS and NASA.

(PDR; Tielens & Hollenbach 1985a). These regions of the interstellar medium are chemically affected by the strong far-ultraviolet (91 nm–240 nm; FUV) radiation emitted by nearby stars, which dissociates molecules and ionizes atoms. Luminous PDRs (such as W49N) are signposts of massive newly formed stars and PDR observations can be used to determine the conditions associated with active massive star formation. Moreover, as argued by Tielens & Hollenbach (1999), PDRs are interesting in themselves because they contain all of the atomic gas and at least 90% of the molecular gas in the Galaxy. Furthermore, PDRs are the origin of much of the IR radiation from the ISM (Tielens & Hollenbach 1999). From luminosity considerations, the PDR emission in W49N is powered by the photon energy from the newly formed massive stars which are also responsible for ionizing the HII regions.

The outline of this paper is as follows. In Sect. 2 we present observations of the continuum and the [OI] and [CII] fine structure lines towards W49N obtained with the ISO-LWS spectrometer, and the $C^{16}O$ ($J = 1 \rightarrow 0$) and $C^{18}O$ ($J = 2 \rightarrow 1$) rotational lines obtained with the SEST telescope. In Sect. 3, the ensemble of these observations is used to characterize the PDR of W49N, namely the average dust temperature, gas density and temperature as well as the illuminating UV field intensity. Section 4 presents the chemical and physical structure of such a PDR, as derived by a detailed PDR model. We finally compare the W49N case to other studied PDRs.

2. Observations and results

2.1. [OI] and [CII] observations

We present observations towards W49N obtained with the *Long Wavelength Spectrometer* (LWS: Clegg et al. 1996) on board the *Infrared Space Observatory* (ISO). We obtained spectra between 43 and 197 μm in grating mode ($\lambda/\Delta\lambda \sim 250$) and high resolution spectra in Fabry-Pérot mode ($\lambda/\Delta\lambda \sim 8000$) of the fine structure lines [CII] 158 μm and [OI] 63 and 145 μm. The $\sim 80''$ ISO-LWS beam (LWS handbook, Gry et al. 2000) was centred on the W49N HII region, namely at: $\alpha_{2000} = 19^{\rm h}10^{\rm m}14^{\rm s}.06$, $\delta_{2000} = 9°06'22.3''$. The data were processed using the Off-Line-Processing pipeline version 7, and the latest improvements of the LIA (LWS Interactive Analysis version 7.3). A final analysis was made using the latest version of the standard package ISAP (version 2.0). Each spectrum was carefully deglitched scan by scan. The continuum level of the FP data was calibrated against observations of the same line of sight with LWS in the grating mode (L01 during revolution 527). L01 spectra are flux calibrated using Uranus, and the absolute accuracy is estimated to be better than 30% (Swinyard et al. 1998).

To separate instrumental effects from real features, we have determined the instrumental response at 158 μm of the LWS-FP in the same way as for the 63 and 145 μm lines described in Vastel et al. (2000), i.e. using the observations towards NGC 7023.

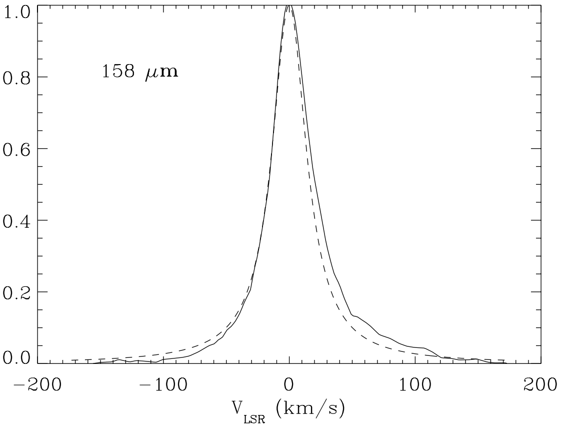

Fig. 1. ISO-LWS FP's instrumental profile (solid line) obtained at 157.741 μm (C^+) using the observations towards the reflection nebula NGC 7023 compared with the theoretical one (dashed line) represented by an Airy profile. Both lines are normalized to unity.

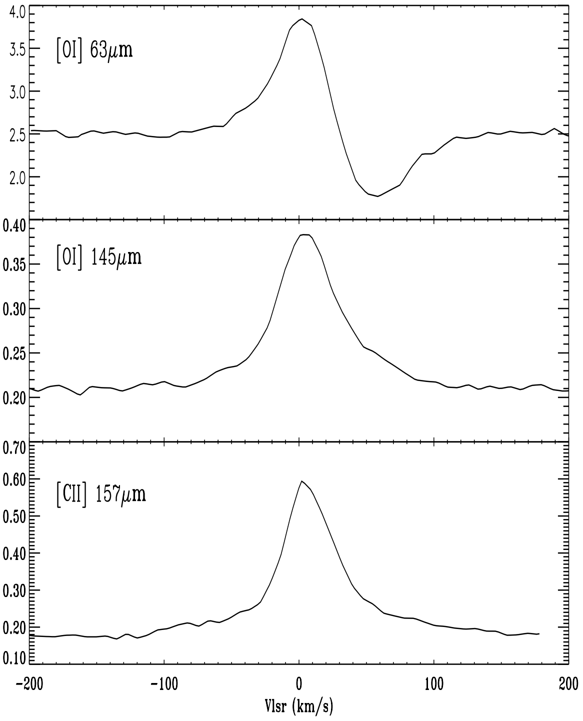

Fig. 2. Observed high resolution spectra of the lines at 63, 145 and 158 μm respectively. Units are in 10^{-8} erg s^{-1} cm^{-2} μm^{-1}. The emission lines are centred at $V_{\rm LSR} = 8$ km s^{-1}.

The derived instrumental profile is shown in Fig. 1: it has a *FWHM* of 37.1 km s^{-1}, slightly larger than the 33.4 km s^{-1} predicted by the instrument optical model. This is probably due to transient effects, as discussed in Vastel et al. (2000).

Figure 2 presents the [OI] 63 μm, 145 μm and [CII] 158 μm line profiles observed in the high spectral resolution mode. Both 145 and 158 μm lines are fitted, before convolution, by a 16 km s^{-1} Gaussian. Note that the 63 μm line contains a strong absorption feature, whose origin is discussed in Vastel et al. (2000) and which affects

Table 1. Measured line fluxes at 145 μm and 158 μm and corrected line flux at 63 μm (see text) from Fabry-Pérot spectra.

Line (μm)	Transition	Flux (10^{-10} erg s^{-1} cm^{-2})
[OI] 63.184	$^3P_1 \rightarrow ^3P_2$	3.7 ± 0.2
[OI] 145.525	$^3P_2 \rightarrow ^3P_3$	0.54 ± 0.06
[CII] 157.741	$^2P_{3/2} \rightarrow ^2P_{1/2}$	1.27 ± 0.09

the emission component at 8 km s^{-1}. Vastel et al. (2000) separated this emission component from the absorption component, which is due to cold molecular clouds and diffuse HI clouds in the velocity range [35 km s^{-1}, 70 km s^{-1}] along the line of sight. In this paper, we focus on the emission component modeled by a 16 km s^{-1} Gaussian linewidth, associated with the HII region of W49N. We disentangled the emission component at 63 μm from the absorption due to diffuse and molecular clouds between -10 km s^{-1} and 100 km s^{-1} with the method described in Vastel et al. (2000). The total absorption component is modeled by the absorption from molecular clouds traced by CO and from diffuse HI clouds where we used a spin temperature of 50 K in the HI clouds (see Brogan & Troland 2001). The corrected line flux at 63 μm and the measured fluxes of the 145 and 158 μm lines are listed in Table 1. Note that the absorption of atomic oxygen from the HI clouds between 0 and 20 km s^{-1} is less than 10% of the total flux of atomic oxygen in emission modeled by Gaussian. We also checked the line fluxes in the grating mode and found that the [OI] 145 μm and [CII] 158 μm lines are similar to the Fabry-Pérot ones at better than 30%.

2.2. CO observations

We observed the C^{16}O $J = 1 \rightarrow 0$ and C^{18}O $J = 2 \rightarrow 1$ lines in May and November 1999 with the 15 meter SEST telescope (ESO – La Silla, Chile). We simultaneously used two SIS receivers at 115 GHz and 230 GHz connected to an Acousto-Optic Spectrometer that provided a spectral resolution of 43 kHz in the two bands (0.105 km s^{-1} and 0.217 km s^{-1} respectively). Typical SSB system temperatures during the observations were 190–250 K and 250–380 K in the two bands respectively. The beam size is 45″ at 115 GHz and 23″ at 230 GHz. Pointing and focus were monitored regularly, and pointing corrections were always found smaller than ∼3″. We performed a five point cross around the nominal position of the W49N HII region, with a 30″ spacing between the points. The goal was to obtain the emission line spectra averaged over the ISO-LWS beam in order to compare C^{16}O, C^{18}O, [OI] and [CII] observations. The CO spectra were therefore convolved with a Gaussian weighting function to degrade the resolution of the SEST beam to 80″. Figure 3 shows the smoothed spectra. The temperatures quoted in this paper are main beam temperatures. It can be noticed that the lines appear in the five point cross around the central position.

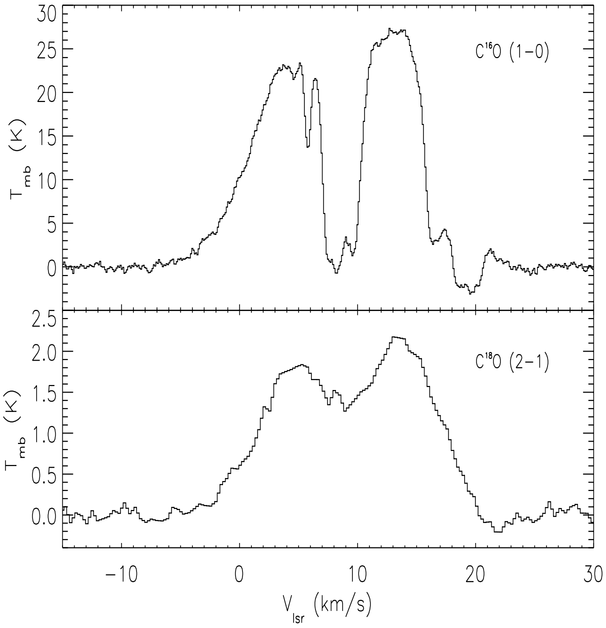

Fig. 3. C^{16}O $J = 1 \rightarrow 0$ and C^{18}O $J = 2 \rightarrow 1$ spectra smoothed to the 80″ LWS beam.

3. Characterisation of the PDR

The goal of this section is to determine the average physical conditions in the PDR of W49N, using simple models to analyze the observed cooling lines. In the following, we will assume that the [OI] and [CII] lines are emitted in the same region dominated by the PDR.

3.1. Source geometry

Given the relatively low spectral and spatial resolution of ISO-LWS we need first to infer indirectly the value of two key parameters, namely the sizes and the linewidth of the line emitting region. Harvey et al. (1977) mapped W49N at 53 μm with a 25″ (*FWHM*) beam. Their cross-section scans in the directions SE-NW and NE-SW gives a continuum source size around 50″. Comparison between the [CII] line emission and the FIR continuum emission in another similar PDR, namely towards the L1630/NGC2024/Orion B cloud (Jaffe et al. 1994; Mookerjea et al. 2000), shows that the C$^+$ region has sizes similar or slightly larger than the continuum region. Assuming therefore that the [OI] and [CII] line extent is similar or larger than the continuum extent, the W49N line emitting region is somewhat larger than 50″ but the emission originates from a region smaller than the LWS beam (80″). This is equivalent to a linear size between 2.8 and 4.5 pc.

The other key observational parameter to constrain is the intrinsic linewidth. In Sect. 2.1 we showed that the [OI] 145 μm and [CII] 158 μm lines have linewidths equal to 16 $\mathrm{km\,s^{-1}}$. Given the large LWS beam, it is likely that such relatively large linewidth is due to the presence of several components in the beam. As mentioned in the Introduction, the radio continuum map of Welch et al. (1987) shows a 2-parsec ring of at least 10 distinct ultracompact HII regions, each associated with at least one O star. From their H76α recombination line observations, they found that the radial velocities of the HII regions are between 14.5 and -2.5 $\mathrm{km\,s^{-1}}$. Therefore, the combination of this ring of spots can give rise to the observed linewidth of 16 $\mathrm{km\,s^{-1}}$ (see Sect. 2.1). Actually, the $\mathrm{C^{18}O}$ spectrum of Fig. 3 confirms the presence of several components in the cloud, whose total velocity dispersion is about 16 $\mathrm{km\,s^{-1}}$. In the following, we will assume that the observed FIR line emission originates in these components and that each cloud component is micro-turbulent pressure supported. We adopt a Doppler b parameter equal to 3.5 $\mathrm{km\,s^{-1}}$, but we remark that the calculated line intensities are not too sensitive to this value.

3.2. The continuum IR emission

From the continuum observations in the grating mode, we can estimate the average dust temperature. As usual, the continuum dust emission from a homogeneous slab can be written in the form:

$$F_\lambda = \Omega_\mathrm{s} \times B_\lambda(T)(1 - \mathrm{e}^{-\tau_\mathrm{dust}}) \quad (1)$$

where Ω_s is the source solid angle, $B_\lambda(T)$ is the blackbody emission at temperature T, and τ_dust is the optical depth. We adopt a $\lambda^{-\beta}$ dust emissivity power law, viz:

$$\tau_\mathrm{dust} = (\lambda_\mathrm{c}/\lambda)^\beta \quad (2)$$

where β is the spectral index, and λ_c is the critical wavelength at which the source becomes optically thin. Figure 4 shows the best fit of our grating spectrum obtained with $T = 43.5$ K, $\beta = 0.9$, and $\lambda_\mathrm{c} = 52$ μm.

The total far-infrared flux of W49N can be calculated by integrating Eq. (1) and with results 1.54×10^{-6} $\mathrm{erg\,s^{-1}\,cm^{-2}}$. At a distance of 11.4 kpc, this corresponds to a total IR luminosity of 6.3×10^6 $L_\odot$, in excellent agreement with the previous estimate (6.8×10^6 $L_\odot$) by Buckley & Ward-Thompson (1996), obtained using observations in a larger wavelength range and with a larger beam size ($145'' \times 130''$).

3.3. [OI] line emission

We have used a Large Velocity Gradient (LVG) code to model the flux of the [OI] lines as functions of the source physical conditions. The details of the code are reported in Ceccarelli et al. (1998). For the present computations, we included also photon pumping by the FIR dust continuum (see Sect. 3.2). The free parameters of the LVG model are: the gas density and temperature, the size of the line emission region, and the column density of atomic oxygen. The dust temperature (43.5 K) and the linewidth (16 $\mathrm{km\,s^{-1}}$) have been derived in the previous sections. The line emitting region will be assumed to be between $50''$ and $80''$ in size, as discussed in Sect. 3.1. The results of our computations are shown in Fig. 5, where we present the 63 μm and 145 μm line emission for three column densities of atomic oxygen, as functions of the gas temperature and density.

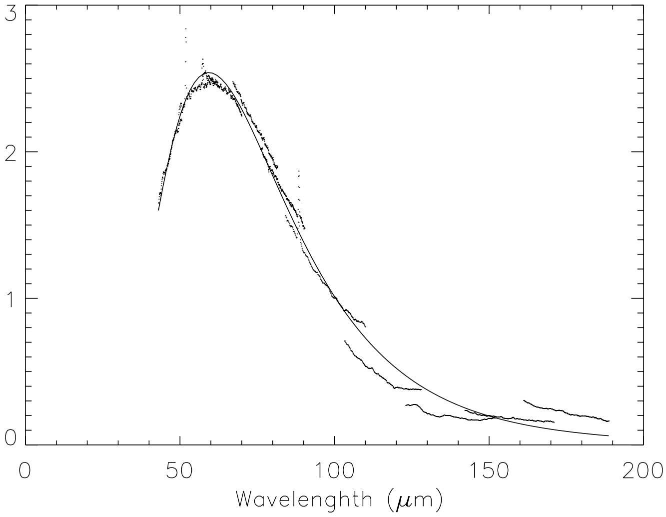

Fig. 4. Comparison between the LWS observed spectrum in the grating mode (dotted line) and the best-fit greybody spectrum (solid line). Units are 10^{-8} $\mathrm{erg\,s^{-1}\,cm^{-2}\,\mu m^{-1}}$.

In order to simultaneously account for the observed [OI] 63 μm and 145 μm line fluxes, the gas temperature has to be $\geq$130 K and the O column density has to be $(5 \pm 3) \times 10^{18}$ $\mathrm{cm^{-2}}$, for a source extent of $50''$, and a factor 2.5 lower for a source extent of $80''$.

3.4. [CII] line emission

In the optically thin limit, the column density of ionized carbon can be derived from the observed line flux with a simple analytic expression as a function of the gas temperature and density. Figure 6 shows the column density of $\mathrm{C^+}$ computed assuming a beam size of $50''$ and $80''$ and a density equal to 10^4 $\mathrm{cm^{-3}}$ for a range of temperatures between 100 and 1000 K. Within this range of temperatures $N(\mathrm{C^+})$ varies between 1.5×10^{18} and 4×10^{18} $\mathrm{cm^{-2}}$ if the source size is $50''$ and it is a factor 2 lower for $80''$. A higher gas density would give the same results since the 158 μm line thermalizes at $\sim 3 \times 10^3$ $\mathrm{cm^{-3}}$ for hydrogen impact excitation, whereas a lower density gas would require larger $\mathrm{C^+}$ column densities. Assuming a minimum gas temperature of 130 K, as estimated in Sect. 3.3, the $\mathrm{C^+}$ column density is $(0.8-2)\times$ 10^{18} $\mathrm{cm^{-2}}$. Note that $\mathrm{O/C^+} \sim 2.5$ if the line is emitted in a $50''$ region, whereas $\mathrm{O/C^+} \sim 1$ if the emitting sizes are rather $80''$. The measured gas phase elemental abundance ratio of O/C is 2.3 in the diffuse ISM (Cardelli et al. 1996; Meyer et al. 1998). Since $\mathrm{C^+}$ and O are the dominant reservoir of carbon and oxygen in a PDR, this would favor a $50''$ source size.

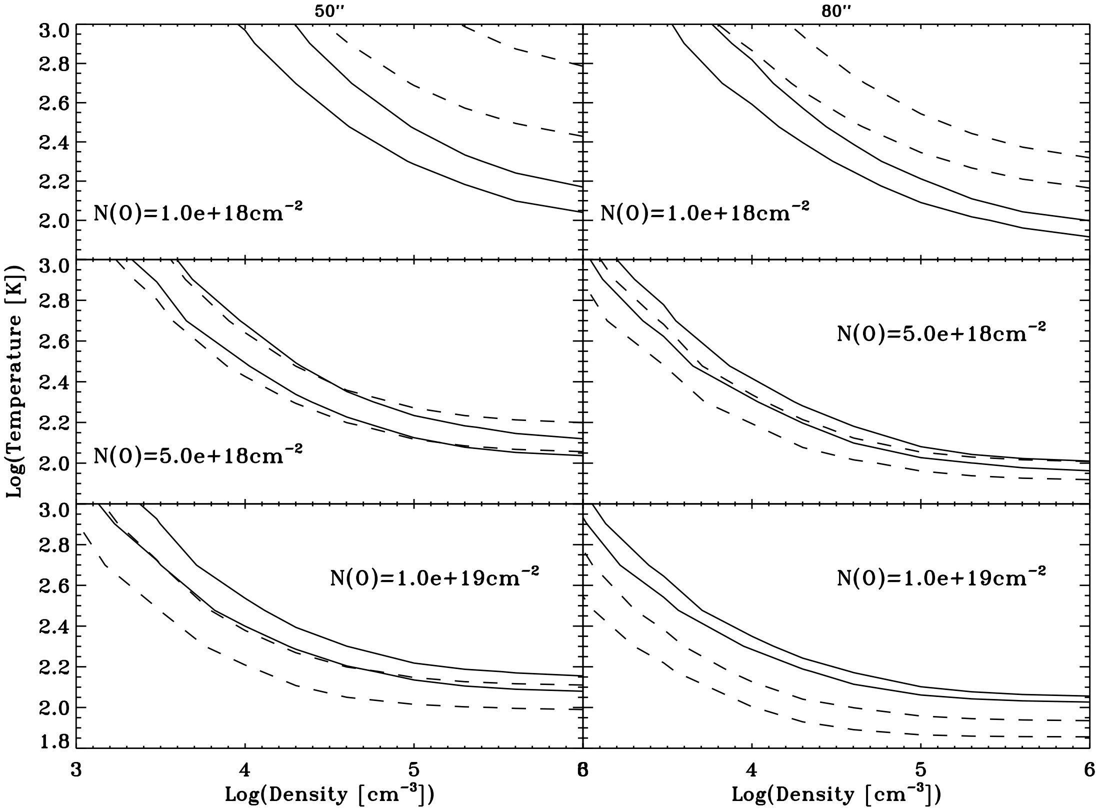

Fig. 5. Temperature versus density plots from our LVG model for a source size of 50″ (left) and 80″ (right) to obtain the fluxes observed in the [OI] 63 μm (solid lines) and 145 μm (dashed lines) respectively for three different oxygen column densities. For each [OI] line, two curves are plotted, which delimit the observed fluxes within a 30% error.

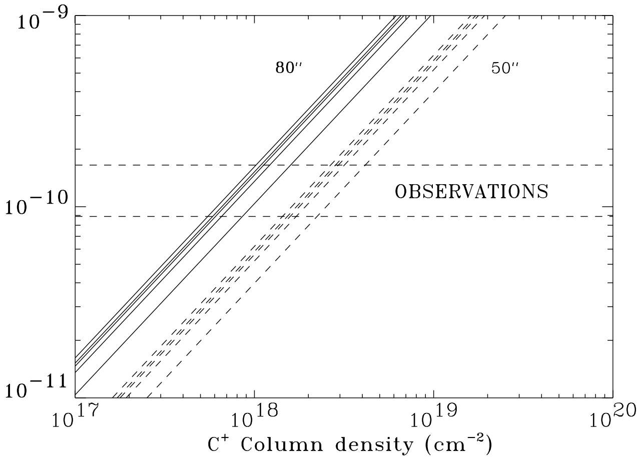

Fig. 6. Computed flux of the [CII] line at 157.741 μm as function of the C$^+$ column density for a density of 10^4 cm^{-3} and temperatures of 100, 200, 300, 400 and 1000 K (from the right to the left) for a source size of 80″ (solid lines) and a source size of 50″ (dashed lines). The horizontal dashed lines represent the 30% error of the observation toward W49N.

3.5. PDR average parameters

In this section we discuss how the [CII], [OI] and CO line emission and line-to-continuum ratio can constrain the physical conditions in the PDR; i.e., the average density and the intensity of the incident FUV radiation field. A method of parameterizing the FUV field incident on a cloud is through G_0, the strength of the 91–240 nm UV radiation field in units of the local interstellar radiation field (Tielens & Hollenbach 1985a). A value of $G_0 = 1$ corresponds to a FUV radiation field of 1.3×10^{-4} erg s^{-1} cm^{-2} sr^{-1}. Assuming that the FUV is the main heating source of the dust, the observed integrated infrared intensity toward W49N (33.5 erg s^{-1} cm^{-2} sr^{-1}) implies $G_0 \sim 3 \times 10^5$, in excellent agreement with the UV flux of the HII regions in W49N, derived from radio observations by De Pree et al. (2000).

Taking the value of $G_0 = 3 \times 10^5$, we can estimate the density of the PDR using the predictions by the Wolfire et al. (1990; hereinafter WTH90) PDR model. They presented especially useful contour plots of the fine-structure emission and line ratios predicted as a function of G_0 and n. Using the observed [CII] 158 μm/[OI] 63 μm line ratio, we derive a density $n \sim 10^4$ cm^{-3} and a G_0/n ratio ~30. In these conditions, the [OI] 63 and 145 μm and [CII] 158 μm lines are expected to be the dominant cooling lines (WTH90). Then the ratio between the derived total line intensity and the FIR continuum intensity yields the grain photoelectric heating efficiency ϵ which is the fraction of FUV photon energy which is converted to gas heating. This value is equal to $(1.4 - 3.6) \times 10^{-4}$ in W49N and is relatively low when compared to that of other studied PDRs, where ϵ is typically 3×10^{-3} (see

Table 4 and the discussion in Sect. 4.3) and implies a relatively large positive grain charge, in agreement with the relatively large G_0/n ratio. In fact a large grain charge implies a high Coulomb barrier that has to be overcome by the photo-ejected electrons and consequently a relatively small fraction of the photon energy carried away by the electrons, reducing the efficiency of the heating mechanism.

Finally, we can estimate the mass in warm atomic gas, M_a, from the observed [CII] 158 μm line flux, following the formalism by WTH90. Taking the values $G_0 = 3\times10^5$ and $n \sim 10^4$ cm^{-3}, we derive an atomic hydrogen column density of $\sim 7\times10^{21}$ cm^{-2} from WTH90 Fig. 6 and an atomic gas mass $M_\mathrm{a} = 600\ M_\odot$. Using our C^{18}O observations we can also estimate the mass of the molecular gas M_{H_2} in the same beam of the [CII] 158 observations. Assuming that the C^{18}O line is optically thin and a ^{16}O/^{18}O ratio equal to 500, we find M_{H_2} = (1–2.5) $\times10^4\ M_\odot$ (e.g. Eqs. (14.115) by Rohlfs & Wilson 1999). This value is in good agreement with previous estimates of the cloud mass ($5\times10^4\ M_\odot$), obtained from 1300 μm continuum emission, C^{18}O ($2\rightarrow1$) and CS ($2\rightarrow1$) observations in a beam larger that our 80″ (Schloerb et al. 1987; Miyawaki et al. 1986). In practice, we find that between 2.4% and 6.2% of the gas mass resides in the warm atomic surface layers of the molecular cloud heated by the newly formed massive stars.

4. Modeling and discussion

4.1. PDR modeling

Here we use a detailed PDR model to determine the physical structure of the PDR whose parameters have been previously derived, namely $G_0 = 3\times10^5$ and $n = 10^4$ cm^{-3}. The physical and chemical properties of a PDR depend on several parameters that may vary over a wide range of possible values; i.e., the molecular hydrogen gas density and pressure, the intensity of the incident FUV radiation field, the absorption and scattering properties of the dust grains, the gas-phase elemental abundances, and the clumpiness of the cloud. The code, described in Spaans (1996) and Spaans & van Dishoeck (1997), has been adopted to a static, plane-parallel, semi-infinite slab which is exposed to an isotropic FUV radiation field in a face-on configuration. In our calculations we assume a constant hydrogen particle density throughout the cloud of 10^4 cm^{-3} and adopt an incident FUV field equal to 3×10^5.

The chemical structure depends on the total gas-phase abundances of the heavy elements. For the volatile elements, carbon and oxygen, we adopt [C] = 1.4×10^{-4} (Cardelli et al. 1996), [O] = 3.2×10^{-4} (Meyer et al. 1998), and [PAH] = 4×10^{-7} (Désert et al. 1990) relative to hydrogen. The photo-destruction rates depend on the incident FUV radiation field and on the cloud depth z, while the cosmic-ray destruction rates depend on the cosmic-ray hydrogen ionization rate. In our model we adopt an interstellar cosmic-ray H$_2$ ionization rate of $\xi = 3\times10^{-17}$ s^{-1} (van der Tak & van Dishoeck 2000). Table 2 lists the set of adopted model parameters.

Table 2. PDR model parameters.

Parameter	Symbol	Value
Hydrogen particle density	n_{H_2} (cm^{-3})	10^4
FUV intensity	G_0	3×10^5
Turbulent Doppler width	b (km s^{-1})	3.5
Carbon abundance	[C]	1.4×10^{-4}
Oxygen abundance	[O]	3.2×10^{-4}
PAH abundance	[PAH]	4×10^{-7}

Table 3. Comparison between the observations of W49N and the PDR model predictions. The lower (respectively upper) limit for the [OI] and [CII] lines corresponds to a 80″ (respectively 50″) line emission size. The CO line intensity is that smoothed in the 80″ beam. Lines that are not observed are labelled as no. The intensities are in erg s^{-1} cm^{-2} sr^{-1}.

	Observations	Model $G_0 = 3\times10^5$ $n_{\mathrm{H}_2} = 10^4$
[OI](63 μm)	$(3.1-8.0)\times10^{-3}$	8.0×10^{-3}
[OI](145 μm)	$(4.6-12)\times10^{-4}$	5.0×10^{-4}
[CII](158 μm)	$(1.1-2.8)\times10^{-3}$	1.4×10^{-3}
[SiII](35 μm)	no	1.9×10^{-4}
[CI](609 μm)	no	1.3×10^{-6}
CO($J=1\rightarrow0$)	4.6×10^{-7}	5.8×10^{-7}
ϵ	$(1.4-3.6)\times10^{-4}$	3.0×10^{-4}

Given all these parameters, the model computes the emergent intensities of the dominant cooling lines including the [CII] 158 μm, [OI] 63 and 145 μm fine structure transitions. The emission of other lines like CO rotational lines, [SiII] 35 μm, [CI] 609 μm are predicted. The model results are compared to the observations in Table 3.

4.2. Results

The lower limit of the observed [OI] 145 μm and [CII] 158 μm lines compares favorably with the model which is consistent with the assumption that the size of the line emitting region is of the order of 80″. In contrast, comparison between the upper limit of the observed [OI] 63 μm line and the model would imply a smaller emitting region of 50″. Assuming this 50″ extend for the cooling lines, the optically thin [CII] 158 μm and [OI] 145 μm lines are somewhat low but still consistent within a factor of two with the observations. This discrepancy is quite common in detailed model fits (cf. Tielens & Hollenbach 1985b) and may reflect geometry effects and/or different dust extinction properties. For example, a viewing angle of 60° rather than face-on would result in a factor 2 increase in the intensity of optically thin lines without affecting much

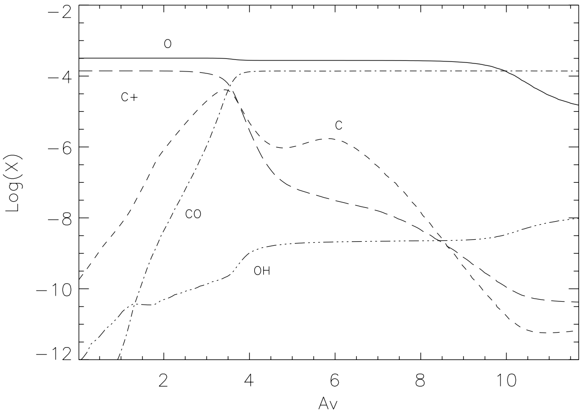

Fig. 7. Abundances of O, C^+, C, CO and OH relative to hydrogen as a function of the depth into the cloud parametrized by the total visual extinction, A_V, for a total hydrogen density of 10^4 cm^{-3} and $G_0 = 3 \times 10^5$.

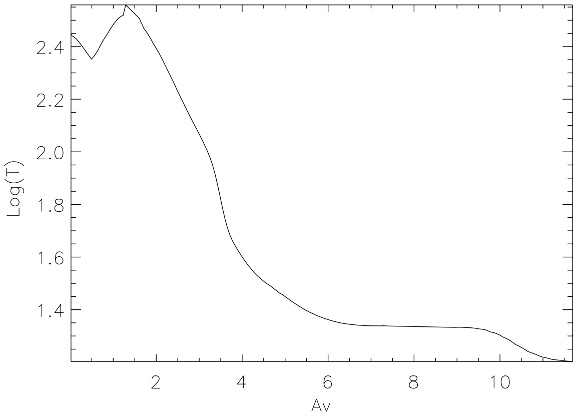

Fig. 8. Thermal profile of the cloud as a function of depth into the cloud parametrized by the total visual extinction, A_V, for a total hydrogen density of 10^4 cm^{-3} and $G_0 = 3 \times 10^5$.

the intensity of optically thick lines (i.e. [OI] 63 μm and CO $J = 1 \rightarrow 0$). Alternatively, a 20% change in the ratio of FUV dust absorption over visual extinction changes the column density of warm gas ($\sim$100 K at $A_v \sim 2$ mag) that emits these lines by a factor of 2.

Figure 7 displays the computed chemical structure of the PDR. The atomic and molecular abundances are sensitive to the cloud depth and many species show distinct abundance peaks at several locations through the cloud. The ionized carbon abundance decreases steadily with depth into the cloud as the FUV flux responsible for the ionization of carbon is attenuated. The CO abundance increases to a level at which most carbon is in the form of CO due to enhanced shielding of CO molecules deeper into the PDRs.

Figure 8 shows the gas temperature as a function of depth into the cloud. The gas temperature initially increases with depth from $T \sim 280$ K at the cloud surface to a maximum of $T \sim 360$ K at $A_V \sim 1.5$. The existence of this temperature peak depends on the decrease of the grain charge with depth into the cloud and on the increase of the optical depth in the main [OI] 63 μm cooling line. Once the grains are largely neutral deeper into the cloud, further FUV attenuation leads to a decrease in the photo-electric heating rate and hence in the temperature. The predicted temperature profile compares well with the average gas temperature derived by the LVG model, i.e. between 250 K and 350 K (see Fig. 5) with a density equal to 10^4 cm^{-3}.

The column densities predicted by the PDR model are: in the warm ($\geq$100 K) surface layers $N(\mathrm{O}) = 4.7 \times 10^{18}$ cm^{-2} and $N(\mathrm{C}^+) = 7.6 \times 10^{17}$ cm^{-2}, while $N(\mathrm{OH}) = 3.9 \times 10^{13}$ cm^{-2} and $N(\mathrm{C}) = 5.9 \times 10^{13}$ cm^{-2} integrating up to $A_V = 10$ mag. We remark that the column densities of the atomic oxygen and ionized carbon computed by the detailed PDR model are in excellent agreement with the estimates of the simpler LVG model.

To summarize, our LVG model in combination with the WTH90 model give estimates of the main parameters of the PDR of W49N, which are confirmed by a detailed PDR model which takes the physics and chemistry of such region fully into account.

4.3. Comparisons with other PDRs

We now compare the PDR of W49N to other studied PDRs associated with HII regions (30 Doradus, M 17, M 42), PDRs associated with reflection nebulae and planetary nebulae (NGC 2068, NGC 7023, NGC 2023, NGC 7027), PDRs associated with the nuclei of a starburst galaxy (M 82), and PDRs associated with the nucleus of our Galaxy. Table 4 lists the observed line fluxes of [OI] 63 μm, [OI] 145 μm, [CII] 158 μm, CO ($1 \rightarrow 0$), the integrated far infrared continuum intensity (FIR) and the computed UV field intensity G_0.

As already mentioned, the UV field in W49N is consistent with the O-5 to O-8 type stars illuminating the several HII regions in the W49N core (De Pree et al. 2000). W49N appears to be one of the most luminous and massive galactic HII regions reflecting an enhanced star formation rate. The compact HII region W49N is a very peculiar source in terms of its heating efficiency which is a factor of $\sim$10 less than most others PDRs (in Table 4) except for the position 2 in the direction of the Galactic Centre, which has very similar characteristics to W49N. The low photoelectric heating efficiency (ϵ) determined for W49N has been explained in the previous sections by a relatively high UV field with respect to the illuminated gas density (G_0/n of $\sim$30).

The ratio between the mass of atomic gas and the molecular gas in W49N, between 2% and 6%, can be compared with the 16% computed for the entire Orion Molecular Cloud (OMC-1) and for the galactic centre (WTH90), and 40% for 30 Doradus which is the most luminous and massive star-forming region in the Large Magellanic Cloud (Poglitsch et al. 1995). This ratio reaches 10% within the central 330 pc for the starburst galaxy M 82 (WTH90), 20% in the reflection nebula NGC 2023 and 30% in the planetary nebula NGC 7027

Table 4. Comparison between W49N and other sources. The line intensities are in erg s^{-1} cm^{-2} sr^{-1}.

Sources	Distance (kpc)	$I(63)$ 10^{-4}	$I(145)$ 10^{-4}	$I(158)$ 10^{-4}	$I(\mathrm{CO}(1–0))$ 10^{-7}	$I(\mathrm{FIR})$	$\mathrm{Log}(G_0)$	ϵ 10^{-4}	References
W49N	11.4	31–80	4.6–12	11–28	4.6	33.5	5.5	1.4–3.6	1
NGC 2023	0.48	36	2.3	6.8	1.5	1.1	4.2	41	2
NGC 7027	1.1	1200	45	130	3.1	60	5.7	23	3
M 82	3300	120	5.3	17	2.7	50	4.7	33	4
Orion Bar	0.47	400	20	60	4	5	4.6	110	5
M17 SW	2.5	150	19	26	7	6.7	4.7	47	6
30 Doradus	49	4.9	0.4	5	0.1	0.6	3.7	17	7
M 42	0.47	400–600	30–60	40–70	5.8	12	5	25	8
NGC 7023	0.43	7.5	0.9	2.8	0.6	0.6	3.7	19	9
NGC 2068	0.48	2.3	0.9	8.1	1.1	0.3	3.4	39	10
Galactic centre 1	8.1	240	6.9	15	2.2–3.0	48	5.6	9.5	11
Galactic centre 2	8.1	40	2.8	8.3	2.2–3.0	17	5.1	4	12

1) This paper. 2) Steiman-Cameron (1997); Milman et al. (1975). 3) Telesco & Harper (1977); Ellis & Werner (1984); Burton et al. (1990). 4) Telesco & Harper (1977); Stacey et al. (1991); WTH90. 5) Tauber et al. (1994). 6) Meixner et al. (1992). 7) Stacey et al. (1991), Poglitsch et al. (1995). 8) Crawford et al. (1985); WTH90. 9) Chokshi et al. (1988), Fuente et al. (2000). 10) Milman et al. (1975); Young Owl et al. (in preparation). 11 and 12) offset of $\Delta b = 0$, $\Delta l = 20''$ for position 1, and $\Delta b = 0$, $\Delta l = 80''$ for position 2, from α_{2000} = 17h 44m 25.52s and $\delta_{2000} = 28°58'1.7''$ (WTH90).

(Tielens & Hollenbach 1999). The comparison between Orion and W49N is particularly instructive, being both galactic massive star forming regions. Since they lie at about the same galactocentric distance they are likely exposed to approximately similar external physical conditions. Therefore, their difference may correspond to a different evolutionary stage. The molecular mass of the gas in the dense star forming core OMC-1 in Orion ($\sim$250 $M_\odot$) is 100 times smaller than in W49N ($\sim 2.5 \times 10^4$ $M_\odot$) (WTH90; De Pree et al. 1997). The total number of Lyman continuum photons is ten times larger in W49N than in Orion although the mass of ionized gas is 6 times larger in Orion than in W49N (Churchwell & Goss 1999; De Pree et al. 1997). A simple explanation is that the O-type stars formed in W49N have only just started to excavate their environment. Moreover, Orion is the classic example of sequential massive star formation where the winds and supernova explosion of one generation of massive stars triggers the formation of the next one (Elmegreen & Lada 1977). W49N seems to be in the earliest stage of this process where the first generation of massive stars has just formed, possibly triggered by the collision of two giant molecular clouds. In conclusion, the W49N complex is one of the youngest star-forming region in the Galaxy since the surrounding molecular cloud has not yet been dispersed by the several embedded newly formed massive protostars.

5. Conclusion

We report observations of [OI] and [CII] lines obtained with LWS on board the ISO satellite in the high resolution spectral mode combined with grating observations. We also present $C^{16}O$ 1 → 0 and $C^{18}O$ 2 → 1 observations obtained with the SEST telescope in the same region encompassed by the ISO-LWS beam.

Using a LVG model and a more sophisticated PDR model we were able to determine the physical structure of the PDR in W49N. This PDR is illuminated by an intense UV field ($G_0 = 3 \times 10^5$) created by the several massive protostars in the cloud. The average gas density of the PDR is 10^4 cm^{-3}. The gas temperature reaches a peak of 360 K at $A_V \sim 1.5$ and decreases to $\sim$22 K in the shielded layers of the cloud.

The photoelectric heating efficiency is very low, $\sim (1.4–3.6) \times 10^{-4}$, when compared with the value of other similar PDRs, $\sim 10^{-3}$. This is probably due to the relatively large UV field with respect to the illuminated gas density, which creates highly charged grains making the photoelectric ejection of the electrons more difficult.

Finally the fraction of the atomic gas in the cloud seems to be smaller than other PDRs, despite the presence of several O stars. This fact suggests that W49N is a relatively young star forming region, where the massive protostars did not yet have time to disperse the cloud.

Acknowledgements. We are grateful to D. Jansen for his assistance with some aspects of the PDR's thermal balance. We acknowledge the dedication of the LWS team which made these observations possible.

References

Brogan, C. L., & Troland, T. H. 2001, ApJ, 550, 799

Buckley, H. D., & Ward-Thompson, D. 1996, MNRAS, 281, 294

Burton, M. G., Hollenbach, D. J., & Tielens, A. G. G. M. 1990, ApJ, 365, 620

Cardelli, J. A., Meyer, D. M., Jura, M., & Savage, B. D. 1996, ApJ, 467, 334

Ceccarelli, C., Caux, E., White, G. J., et al. 1998, A&A, 331, 372

Chokshi, A., Tielens, A. G. G. M., Werner, M. W., & Castelaz, M. W. 1988, ApJ, 334, 803

Churchwell, E., & Goss, W. 1999, ApJ, 514, 188

Clegg, P. E., Ade, P. A. R., Armand, C., & Baluteau, J.-P. 1996, A&A, 315, 38

Crawford, M. K., Genzel, R., Townes, C. H., & Watson, D. M. 1985, ApJ, 291, 755

de Pree, C. G., Mehringer, D. M., & Goss, W. M. 1997, ApJ, 482, 307

de Pree, C. G., Wilner, D. J., Goss, W. M., et al. 2000, ApJ, 540, 308

Désert, F. X., Boulanger, F., & Puget, J. L. 1990, A&A, 237, 215

Ellis, H. B., & Werner, M. W. 1984, AAS, 16, 463

Elmegreen, B. G., & Lada, C. J. 1977, ApJ, 214, 725

Fuente, A., Martin-Pintado, J., Rodriguez-Fernandez, N. J., et al. 2000, A&A, 354, 1053

Gry, C., on behalf of the LWS Consortium 2000, LWS Handbook

Gwinn, C. R., Moran, J. M., & Reid, M. J. 1992, ApJ, 393, 149

Harvey, P. M., Campbell, M. F., & Hoffmann, W. F. 1977, ApJ, 211, 786

Jaffe, D. T., Zhou, S., Howe, J. E., et al. 1994, ApJ, 436, 203

Meixner, M., Haas, M. R., Tielens, A. G. G. M., et al. 1992, ApJ, 390, 499

Meyer, D. M., Jura, M., & Cardelli, J. A. 1998, ApJ, 493, 222

Milman, A. S., Knapp, G. R., Knapp, S. L., & Wilson, W. J. 1975, AJ, 80, 93

Miyawaki, R., Hayashi, M., & Hasegawa, T. 1986, ApJ, 305, 353

Mookerjea, B., Ghosh, S. K., Rengarajan, T. N., Tandon, S. N., & Verma, R. P. 2000, AJ, 120, 1954

Mufson, S. L., & Liszt, H. S. 1977, ApJ, 212, 664

Poglitsch, A., Krabbe, A., Madden, S. C., et al. 1995, ApJ, 454, 293

Rohlfs, K., & Wilson, T. L. 1999, Tools of Radio Astronomy, Third revised and enlarged edition (Springer)

Schloerb, F. P., Snell, R. L., & Schwartz, P. R. 1987, ApJ, 319, 426

Serabyn, E., Guesten, R., & Schultz, A. 1993, ApJ, 413, 571

Spaans, M. 1996, A&A, 307, 271

Spaans, M., & van Dishoeck, E. 1997, ApJ, 323, 953

Stacey, G. J., Geis, N., Genzel, R., et al. 1991, ApJ, 373, 423

Steiman-Cameron, T. Y., Haas, M. R., & Tielens, A. G. G. M. 1997, ApJ, 478, 261

Swinyard, B. M., Burgdorf, M. J., Clegg, P. E., et al. 1998, SPIE, 3354, 888

Tauber, J. A., Tielens, A. G. G. M., Meixner, M., & Goldsmith, P. F. 1994, ApJ, 422, 136

Telesco, C. M., & Harper, D. A. 1977, ApJ, 211, 475

Tielens, A. G. G. M., & Hollenbach, D. 1985a, ApJ, 291, 722

Tielens, A. G. G. M., & Hollenbach, D. 1985b, ApJ, 291, 747

Tielens, A. G. G. M., & Hollenbach, D. 1999, Rev. Mod. Phys., 71, 173

van der Tak, F. F. S., & van Dishoeck, E. F. 2000, A&A, 358, 79

Vastel, C., Caux, E., Ceccarelli, C., Castets, A., et al. 2000, A&A, 357, 994

Webster, W. J., Altenhoff, W. J., & Wink, J. E. 1971, AJ, 76, 677

Welch, W. J., Dreher, J. W., Jackson, J. M., Terebey, S., & Vogel, S. N. 1987, Science, 238, 1550

Wolfire, M. G., Tielens, A. G. G. M., & Hollenbach, D. 1990, ApJ, 358, 116

Wynn-Williams, C. G. 1971, MNRAS, 151, 397

Young Owl, R. C., Meixner, M. M., Fong, D., et al. 2001, in preparation